A computational tool for the detailed kinetic modeling of laminar flames: Application to C_2H_4/CH_4 coflow flames

Alberto Cuoci *, Alessio Frassoldati, Tiziano Faravelli, Eliseo Ranzi

Department of Chemistry, Materials, and Chemical Engineering, Politecnico di Milano, P.zza Leonardo da Vinci 32, 20133 Milano, Italy

ABSTRACT

In this work a new computational framework for the modeling of multi-dimensional laminar flames with detailed gas-phase kinetic mechanisms is presented. The proposed approach is based on the operator-splitting technique, in order to exploit the best numerical methods available for the treatment of reacting, stiff processes. The main novelty is represented by the adoption of the open-source `OpenFOAM`® code to manage the spatial discretization of the governing equations on complex geometries. The resulting computational framework, called `laminarSMOKE`, is suitable both for steady-state and unsteady flows and for structured and unstructured meshes. In contrast to other existing codes, it is released as an open-source code and open to the contributions from the combustion community.

The code was validated on several steady-state, coflow diffusion flames (fed with H_2, CH_4 and C_2H_4), widely studied in the literature, both experimentally and computationally. The numerical simulations showed a satisfactory agreement with the experimental data, demonstrating the feasibility and the accuracy of the suggested methodology. Then, the C_2H_4/CH_4 laminar coflow flames experimentally studied by Roesler et al. [J.F. Roesler et al., Combust. Flame 134 (2003) 249–260] were numerically simulated using a detailed kinetic mechanism (with ∼220 species and ∼6800 reactions), in order to investigate the effect of methane content on the formation of aromatic hydrocarbons. Model predictions were able to follow the synergistic effect of the addition of methane in ethylene combustion on the formation of benzene (and consequently PAH and soot).

© 2013 The Combustion Institute. Published by Elsevier Inc. All rights reserved.

1. Introduction

Numerical simulations of laminar flames have received a widespread interest in the past two decades, since they can be used for the design and optimization of industrial and domestic equipment (e.g. furnaces, domestic gas burners, industrial burners, etc.), and for the understanding and modeling of more complex flows (e.g. turbulent flames). However, the modeling of multi-dimensional laminar flames with realistic chemical mechanisms represents a challenging problem and places severe demands on computational resources, mainly because of the large number of chemical species involved, the high stiffness of the governing equations and the presence of high gradient regions (especially close to the flame front) [1]. When detailed kinetic schemes are used, special attention must be devoted to the numerical algorithms, which must be very efficient and accurate. At the same time, the spatial discretization has to be fine enough to adequately describe the flame fronts and the high gradients. Consequently, the computational effort in terms of CPU time and memory requirements is considerable and often prohibitive.

Conventional CFD methods based on segregated algorithms have serious difficulties in treating the stiffness and the high non-linearities of the governing equations and cannot be efficiently applied in this context. In order to overcome these problems, coupled methods appear to be an attractive alternative. In particular, among others, two main numerical approaches have been used for the resolution of such a stiff, large system of equations: (i) fully coupled algorithms [2]; (ii) algorithms based on operator-splitting methods [3–7]. An advantage of fully coupled algorithms is that all the processes are considered simultaneously, so all physical interactions among processes are taken into account together (and therefore this seems the natural way to treat problems with multiple stiff processes). However, the resulting system of governing equations can be extremely large (especially when detailed kinetic mechanisms and complex, multi-dimensional geometries are considered). When operator-splitting methods are used, the governing equations are split in sub-equations, usually with each having a single operator, capturing only a portion of the physics present. Splitting approaches can be conveniently applied for the numerical solution of combustion problems, by separating the stiff chemical

* Corresponding author. Fax: +39 02 7063 8173.
  E-mail address: alberto.cuoci@polimi.it (A. Cuoci).

reaction processes from the non-stiff transport processes. An advantage of this approach is that it usually avoids many costly matrix operations (typical of fully coupled algorithms) and allows the best numerical method to be used for each type of term or process. A potential disadvantage with respect to fully coupled methods is that separate algorithms can be very complex and usually differ from term to term and even from one situation to another. The exact way the processes are coupled, therefore, may also vary for different types of problems.

Several, excellent solvers for reactive, laminar flames were developed in the last years. Ern et al. [8] developed a low-cost numerical framework for solving low-Mach-number reactive flows, on the basis of a velocity–vorticity formulation. An efficient, fully-coupled method is adopted and good performances on multiprocessor architectures are achieved via a domain decomposition method. Several improvements were introduced, both about numerical aspects [9–11] and about physical sub-models (e.g. radiative heat transfer and soot formation [12]). However, one drawback of the velocity–vorticity formulation is the difficulty in accurately treating boundary conditions and the possibility to solve only 2D flows [11].

Knio et al. [13] developed a stiff operator split projection scheme for simulating unsteady 2D reacting flows with detailed kinetics. The full numerical methodology was applied for modeling the interaction of a premixed methane/air flame with a counter-rotating vortex pair, using the GRI 1.2 mechanism (32 species and 177 reactions) [14], with excellent results in terms of accuracy and stability. However, to our knowledge, the solver has not been applied for the simulation of laminar coflow flames with very detailed kinetic mechanisms.

D'Anna and coworkers [15] developed a numerical framework for solving laminar, axisymmetric flames. The solver is based on the alternating-direction implicit (ADI) scheme and a tri-diagonal matrix algorithm (TDMA) to solve the linearized equations. The solver was used especially for the prediction of formation of PAHs and soot in laminar coflow flames, but unfortunately only a few details about the adopted numerical algorithms are provided by the authors.

The numerical framework proposed by Liu et al. [16] and Guo et al. [17] solves the governing equations on structured meshes using a SIMPLE finite volume scheme, which decouples the mass and momentum equations to deal with pressure–velocity couplings [18]. A segregated approach based on the TDMA is used to solve the equations of total mass, momentum and energy. Then, equations of individual species are solved with a multigrid method, but, as reported by the authors, this method cannot be applied for time-accurate studies.

Day and Bell [5] developed a very efficient, parallel algorithm, for both steady-state and unsteady reacting flows in the low-Mach-number limit, in complex geometries. A fractional step method and adaptive mesh refinement (AMR) are adopted to solve the equations on a single grid. Excellent parallel performances were observed (especially for turbulent flames).

More recently, Charest et al. [19] proposed a new computational framework, specifically conceived for multiprocessor computer architectures. The governing equations for compressible flows are solved for all speeds with a Newton–Krylov-based implicit solver. Discretization uses a second-order accurate finite volume scheme, together with a parallel AMR on body-fitted, multiblock meshes. The algorithm was applied with good results to laminar coflow flames, showing excellent scaling performances.

Dobbins and Smooke [20], focused the attention on the numerical modeling of multidimensional, time-dependent laminar flames. In particular, a fully implicit numerical method based on a high-order compact finite difference spatial discretization was used for simulating a periodically forced axisymmetric laminar

jet diffusion flame. It was demonstrated the importance of adopting a very high-order spatial discretization to correctly capture all the unsteady phenomena and the superior performance of the proposed methodology with respect to a variety of low-order numerical methods, including some that are locally adaptive in space. However, in this work only a one-step kinetic mechanism was used for the calculations.

Most of the codes reported above are based on the finite volume (FV) or finite difference (FD) techniques. However, several authors, especially in recent years, focused the attention on the application of the finite element (FE) method in complex geometries and/or unstructured grids, to exploit the possibility to automatically and adaptively refine the computational mesh, with possible estimation of the discretization error. Among the others, Becker et al. [21] performed numerical simulation of laminar flames at low Mach number with adaptive finite elements and detailed kinetic schemes. Burman et al. [22] focused their attention on the simulation of reacting flows with finite elements on unstructured triangulations, adaptively refined using a posteriori error estimate derived from the dual weighted residual method. Numerical results were presented for a Bunsen flame and a complex hydrogen/air chemistry was adopted.

In the present work a new framework (called `laminarSMOKE`) for the numerical modeling of laminar, reactive flows is presented, based on the operator-splitting methodology and specifically conceived for very detailed kinetic mechanisms (hundreds of species). The main novelty is represented by the adoption of the well-known, open-source `OpenFOAM`® code [23] to efficiently manage the computational meshes and the discretization process of the governing equations. The stiff features of the governing equations is managed through the `BzzMath` [24,25] and the `OpenSMOKE` [26,27] libraries. The resulting code can be used for steady-state and unsteady flows, in complex grids (structured and unstructured) and is freely available and open to new contributions from the combustion community.[1]

The purpose of this work is twofold: on one hand the description of the new computational code and the demonstration of its reliability and accuracy for the modeling of laminar flames; on the other hand, the application of the proposed computational code to the numerical simulation of a set of C_2H_4/CH_4 laminar coflow flames, in order to investigate the effect of methane on the formation of aromatic hydrocarbons.

The organization of the paper reflect this twofold objective. In Section 2 we introduce the mathematical model and the numerical algorithms employed by the `laminarSMOKE` code. In Section 3 the framework is validated via comparison with experimental data on several laminar coflow flames, widely studied (experimentally and numerically) by different research group. Then, in Section 4 the `laminarSMOKE` code is used to study the formation of aromatic hydrocarbons in a series of laminar coflow flames (fed with a mixture of C_2H_4 and CH_4), experimentally studied by Roesler et al. [28]. The final section presents some conclusions and discusses future developments.

2. Numerical methodology

2.1. Governing equations

The reactive, laminar flows under investigation in the present work are mathematically described by the conservation equations for continuous, multicomponent, compressible, thermally-perfect mixtures of gases [19]. The conservation equations of total mass,

---

mixture momentum, individual species mass fractions and mixture energy, are reported in the following (assuming a Newtonian fluid):

$$\frac{\partial \rho}{\partial t} + \nabla(\rho \mathbf{v}) = 0 \tag{1}$$

$$\frac{\partial}{\partial t}(\rho \mathbf{v}) + \nabla(\rho \mathbf{vv} + p\mathbf{I}) = \nabla \tau + \rho \mathbf{g} \tag{2}$$

$$\frac{\partial}{\partial t}(\rho \omega_k) + \nabla(\rho \omega_k \mathbf{v}) = -\nabla(\rho \omega_k \mathbf{V}_k) + \dot{\Omega}_k \quad k = 1, ..., NC \tag{3}$$

$$\rho C_P \frac{\partial T}{\partial t} + \rho C_P \mathbf{v} \nabla T = -\nabla \mathbf{q} - \rho \sum_{k=1}^{NC} C_{P,k} \omega_k \mathbf{V}_k - \sum_{k=1}^{NC} h_k \dot{\Omega}_k \tag{4}$$

where t is the time, ρ is the mixture density, p the pressure, $\mathbf{v}$ the mixture velocity vector, τ the fluid stress tensor, $\mathbf{g}$ the acceleration vector due to gravity, ω_k the mass fraction of species k, $\mathbf{V}_k$ is the diffusion velocity of species k, $\dot{\Omega}_k$ the formation rate of species k, T the temperature, C_P and $C_{P,k}$ are the specific heat at constant pressure of the mixture and of the individual species k, respectively, $\mathbf{q}$ the heat flux vector and h_k the individual species enthalpy.

The density of the mixture is calculated using the equation of state of ideal gases. The heat flux vector accounts for conduction and radiation:

$$\mathbf{q} = -\lambda \nabla T + \mathbf{q}_{rad} \tag{5}$$

where λ is the mixture thermal conductivity and $\mathbf{q}_{rad}$ the radiative heat flux. Both Fickian and thermal diffusion are taken into account for evaluating the diffusion velocities [29]:

$$\mathbf{V}_k = -\frac{\Gamma_k}{\omega_k} \nabla \omega_k - \frac{\Gamma_k \Theta_k}{X_k} \frac{1}{T} \nabla T \tag{6}$$

where Γ_k is the individual species mixture averaged diffusion coefficient, X_k the mole fraction and Θ_k the thermal diffusion ratio of species k. Mass conservation is enforced by employing the approach proposed by Coffee and Heimerl [30], based on the definition of a *correction diffusion velocity*. In particular, in this approach the corrected diffusion velocity vector $\mathbf{V}_k^C$ (to be used in Eqs. (3) and (4)) is given as:

$$\mathbf{V}_k^C = \mathbf{V}_k + \mathbf{V}_C \tag{7}$$

where $\mathbf{V}_C$ is a constant correction factor (independent of species, but varying in space and time) introduced to satisfy the mass conservation and evaluated as:

$$\mathbf{V}_C = -\sum_{k=1}^{NC} \omega_k \mathbf{V}_k \tag{8}$$

Of course the adoption of the Fick's law and the *light species approximation* for the evaluation of the thermal diffusion ratios could result in some inaccuracies. A full multicomponent approach should be employed in order to improve the accuracy and enforce the conservation of mass without any corrections. Multidimensional flame simulations with with computationally efficient implementations of full multicomponent transport models have already been performed [31], but the evaluation of transport properties through such models is so computationally expensive, that most of the works about the numerical simulations of laminar co-flow flames reported in the literature prefer to adopt the less accurate (but less expensive) mixture averaging rules. Therefore, as evidenced by the satisfactory agreement with experimental data (Sections 3 and 4), we are quite confident that the simple mixture averaging formulation (Eq. (6)) is sufficiently reliable and accurate for the purposes of the present paper. In addition, the correction diffusion velocity has been justified from a theoretical point of

view, that is, the Hirschelder–Curtiss approximation with the correction velocity is the first term of a convergent series expansion of the Stefan–Maxwell velocities [32]. Moreover, In the future we would like to remove this limitation by adding the possibility to calculate the gas mixture properties using a full multicomponent approach, following the work of Dixon–Lewis [33].

An optically thin radiation model is included in the calculations. For the mixtures here considered, it is assumed that the only significant radiating species are H_2O, CO, CO_2 and CH_4. By adopting an optically thin limit in which self-absorption of radiation is neglected, the divergence of the net radiative flux can be written as:

$$\nabla \mathbf{q}_{rad} = -4\sigma a_P (T^4 - T_{env}^4) \tag{9}$$

where σ is the Stefan–Boltzmann constant and T_{env} the environment temperature. The Planck mean absorption coefficient a_P is evaluated according to the following expression:

$$a_P = p_{H_2O} a_{p,H_2O} + p_{CO_2} a_{p,CO_2} + p_{CO} a_{p,CO} + p_{CH_4} a_{p,CH_4} \tag{10}$$

where p_k is the partial pressure of species k. The extinction coefficient $a_{p,k}$ of species k is derived from calculations performed by the RADCAL software [34].

2.2. Splitting algorithm

The OpenFOAM® framework [23] is used to solve the gas-phase transport equations reported above. The standard OpenFOAM® solver for compressible, unsteady, non-reacting flows, called piso-Foam, was modified in order to make possible the introduction of detailed kinetic mechanisms. In particular, an operator-splitting approach, based on the separation of transport and reaction terms, was implemented, as briefly described in the following.

After spatial discretization, the transport equations of mass species and energy, can be written in the general form [35]:

$$\frac{d\psi}{dt} = \mathbf{S}(\psi) + \mathbf{M}(\psi, t) \tag{11}$$

where ψ is the vector of dependent (or primary) variables (here, mass fractions and temperature), $\mathbf{S}(\psi)$ the vector of rates of change of ψ due to chemical reactions and $\mathbf{M}(\psi, t)$ the vector of rates of change of ψ due to transport processes (such as diffusion, convection, heat loss, inflow/outflow, etc.). In order to solve Eq. (11) numerically, the time is discretized in increments Δt, and the integration in time is then performed using the Strang splitting scheme [36]. According to this approach, reaction is separated from the transport process and the numerical integration is performed in three sub-steps:

Sub-step 1. The reaction terms are integrated over the interval $\Delta t/2$, through the solution of the ODE system:

$$\frac{d\psi^a}{dt} = \mathbf{S}(\psi^a) \tag{12}$$

The initial condition $\psi^a(0)$ is equal to the final state from the previous time step and the solution of Eq. (12) is indicated as $\psi^a(\Delta t/2)$.

Sub-step 2. The transport terms (convection and diffusion) are integrated over the interval Δt by solving:

$$\frac{d\psi^b}{dt} = \mathbf{M}(\psi^b, t) \tag{13}$$

The initial condition $\psi^b(0)$ corresponds to the final state of the system from the Sub-step 1, $\psi^a(\Delta t/2)$, and the solution of Eq. (13) is denoted by $\psi^b(\Delta t)$.

Sub-step 3. This step is identical to Sub-step 1, with the exception that the initial condition corresponds to the final state of

the system from Sub-step 2, $\psi^b(\Delta t)$. The solution is used as the initial condition for the next time step.

The reaction operator $\mathbf{S}(\psi)$ is independent of time and does not involve any discretization operation in space, which means that reaction process is local (separate for each grid point). On the contrary, the transport operator $\mathbf{M}(\psi, t)$ may depend on time if boundary conditions are time-dependent. More important, $\mathbf{M}(\psi, t)$ is not separate for different grid points, which are coupled by the convection and diffusion terms. As a consequence, Sub-steps 1 and 3 correspond to N independent stiff ODE systems, in $NC + 1$ unknowns (species mass fractions and temperature), where N is the total number of computational cells and NC the number of species. Such uncoupled ODE systems are conveniently integrated over the requested time step using the `BzzOde` solver [24], which is specifically conceived for very stiff ODE systems arising from the numerical modeling of reactive systems with detailed kinetics [37]. Sub-step 2 correspond to an ODE system of $N(NC + 1)$ coupled equations. However, since these equations are not stiff (the chemical reactions are considered only in Sub-steps 1 and 3), the solution is performed in a segregated approach: instead of solving the whole ODE system, $NC + 1$ ODE systems are solved in sequence, each of them having dimension equal to N. The `OpenFOAM`® framework is used to manage the spatial discretization of transport terms and to solve the Eq. (13) using the implicit Euler method. In particular, the linear systems involved in this process are solved through iterative techniques, i.e. reducing the equation residual over a succession of solutions [38]. The PBiCG (Preconditioned Conjugate Gradient) method is adopted for all the linear systems, with the exception of the Poisson equation for the pressure, which is solved using the PCG (Preconditioned Conjugate Gradient) method, because of the symmetry of the corresponding linear system. The PBiCG method is preconditioned through the DILU (Diagonal incomplete-LU) technique, while the PCG method is preconditioned by the DIC (Diagonal Incomplete Cholesky). The solver stops if either of the following conditions are reached: a) the residual falls below the absolute solver tolerance; b) the ratio of current to initial residuals falls below the solver relative tolerance; c) the number of iterations exceeds a maximum number of iterations. The absolute tolerance is usually set equal to 10^{-7}. For steady-state simulations a relative tolerance of 10^{-3} is assumed, while in transient simulations, it is usual to set the relative tolerance equal to 0 to force the solution to converge to the absolute tolerance in each time step, in order to have a better accuracy.

The splitting procedure described above is applied only to species and energy equations. The continuity and momentum equations are solved in a segregated approach, using the PISO algorithm, already available in `OpenFOAM`® [39]. The whole numerical procedure is summarized in Fig. 1. The time-step is automatically adapted to keep the Courant number sufficiently low in every computational cell, in order to avoid stability issues. In particular, the simulations reported in this work were performed imposing a maximum Courant number equal to 0.1.

The numerical properties of operator splitting approaches for the solution of transport equations with stiff chemistry were studied by several authors [6,40,41]. In particular, it seems evident that the operator sequence is crucial to obtain satisfactory stability and accuracy and that the stiff (chemistry) operator has always to be last in the splitting process.

The `laminarSMOKE` code runs both in sequential and parallel mode on distributed-memory machines. In particular, it employs the Domain Decomposition Method to split the mesh into a number of sub-domains and allocate them to separate processors. The code can then run in parallel on separate sub-domains, with communication between processors with MPI communication protocol. Since most of the computational time (~90%) is spent for the
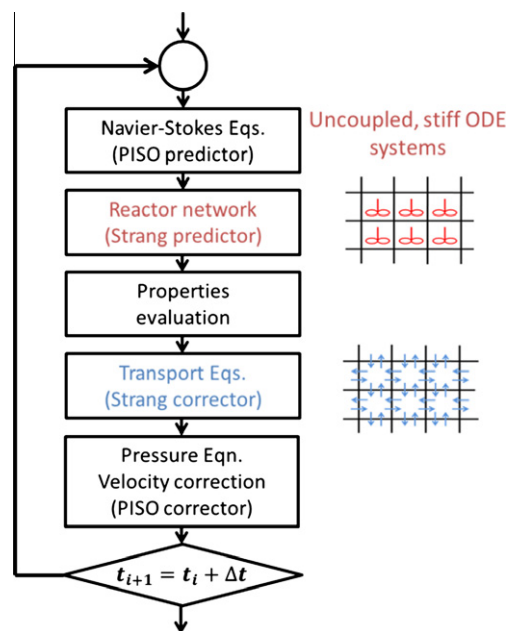

Fig. 1. Numerical algorithm used in `laminarSMOKE`.

integration of the chemical step, which does not require communication between the different sub-domains, the parallel performances of the `laminarSMOKE` code are satisfactory, with efficiency (defined as $\frac{t_S}{pt_P}$, with p equal to the number of processors, t_S and t_P the execution times on a single processor and with p processors, respectively) of 60–70% for the coflow flames investigated in this work.[2]

2.3. Detailed kinetic mechanisms

Several detailed kinetic mechanisms, developed at the Politecnico di Milano and extensively described and validated in [42,43], were used in the present work. In particular, hydrogen flames were simulated with the `POLIMI_H2CO1211` mechanism, consisting of 14 species and 37 reactions [44]. Methane and ethylene flames were calculated using the `POLIMI_C1C31211NOx` scheme (111 species and 1862 reactions) or the more general `POLIMI_HT1211` (187 species and 6117 reactions) and `POLIMI_HT1211NOx` (222 species and 6856 reactions) schemes, accounting also for the formation of soot precursors. All the kinetic mechanisms are freely available in CHEMKIN format (together with thermodynamic data and transport properties) at http://creckmodeling.chem.polimi.it/.

Transport properties (mass diffusion coefficients, thermal conductivity and viscosity) are taken from the CHEMKIN transport database [45] or estimated following the procedure proposed by Wang and Frenklach [46]. The thermochemical data on the gas phase was obtained primarily from the CHEMKIN thermodynamic database. Unavailable thermodynamic data were estimated by group additivity methods [47].

3. Validation for coflow flames

The numerical procedure described in the previous Section was verified through the simulation of several premixed, flat laminar

---

[2] Further details about the parallelization strategy and the corresponding computational efficiency (together with description of the programming techniques employed to build the code) will be the subject of a dedicated paper which is in preparation (Journal of Computational Physics).

flames, for which accurate numerical solutions (obtained using a fully-coupled algorithm) were available. The Appendix A provides a short overview of the verification procedure, applied to study the reliability and the accuracy of the proposed framework. In this paragraph only the details about the validation procedure are summarized.

Since the discretization of the transport equations is managed by the OpenFOAM® framework, the `laminarSMOKE` solver can be applied to very general reacting flows with detailed kinetics in arbitrarily complex geometries (2D and 3D), in steady-state and unsteady conditions. In this paper we did not exploit all these features and capabilities, since we were mainly interested in validating the numerical methodology. Therefore we focused our attention on axisymmetric, laminar coflow flames, mainly because of the availability of a large amount of accurate experimental measurements (temperature, major and minor species). Of course in the future, additional, more complex cases have to be tested, both in terms of numerical verification and validation with respect to the experimental measurements.

Several laminar coflow flames were numerically investigated: (i) a couple of flames fed with a mixture of H_2/N_2 in air, experimentally studied by Toro et al. [48]; (ii) the methane/air flame experimentally and computationally studied by Bennett et al. [49]; (iii) the ethylene/air flame investigated by McEnally and Pfefferle [50] and extensively modeled by Bennet et al. [51]; (iv) the lifted methane/air flame experimentally and numerically studied by by Smooke et al. [52] and McEnally et al. [53]. For all the flames considered in this Section, a 2D rectangular domain, initially meshed with a structured grid, was considered. The fuel velocity profile was always assumed parabolic, while a flat velocity profile was imposed for the coflow stream.

3.1. H_2/N_2 coflow flames

The H_2/N_2 flames experimentally studied by Toro et al. [48], were chosen as a first test-case for the validation of the numerical code, because the fuel is H_2, whose chemistry is well-known and can be described with a relatively small number of species. The fuel nozzle has an internal diameter of 9 mm and is surrounded by an air-coflow annulus (i.d. 95 mm). The fuel stream is a mixture of 50% H_2 and 50% N_2 (by volume) at ambient temperature. Two different average fuel exit velocities are considered in the present work: 27 cm/s (Flame F2) and 50 cm/s (Flame F3). Measurements of temperature, H_2, O_2, H_2O and OH mole fractions are available along the axis and in radial direction at 3, 10, 20 and 30 mm from the fuel nozzle.

The computational domain has a width of 95 mm and a length of 150 mm. Computations are performed on grids with three levels of refinement, containing respectively 3000, 6000 and 12,000 cells. The hydrogen–oxygen chemistry was described using the POLIM-I_H2CO1211 kinetic scheme [44].

Figure 2 reports an example of the computational mesh here used, together with the calculated maps of temperature and mass fractions of O_2 and H_2O, in order to better show the computational domain and the main structural properties of the investigated flames. Figure 3 reports the comparison between predictions and measurements along the center-line in terms of temperature. The results refer to the mesh with 6000 cells, which was found fine enough for the validation here proposed. The agreement is quite satisfactory, especially for Flame F3. This can be partially attributed to the larger heat transfer to the fuel tube in flame F2, which makes the temperature and composition at the fuel exit more difficult to be predicted, increasing the uncertainty in the corresponding boundary condition [48]. The computations over-estimate the temperature peak of ~75 K, but the overall agreement is reasonable, especially considering the simplicity of the radiative heat
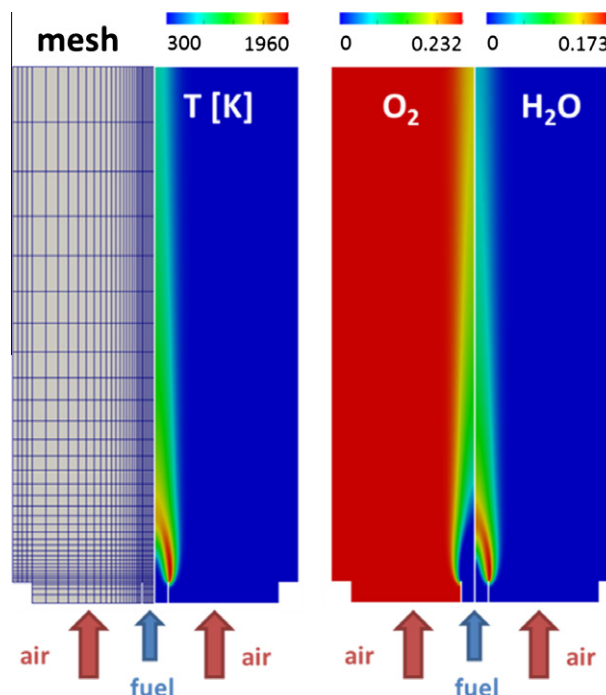

Fig. 2. H_2/N_2 coflow flames: computational mesh and 2D maps of temperature and mass fractions of O_2 and H_2O for H_2/N_2 coflow flame (Flame F2). The mesh is here presented with a reduced number of cells for graphical reasons.
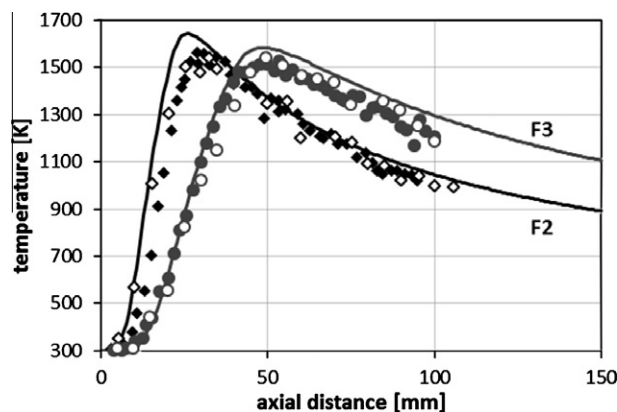

Fig. 3. H_2/N_2 coflow flames: comparison between experimental measurements [48] and numerical temperature profiles in axial direction.

transfer model here employed. Additional comparisons along the axis are presented in Fig. 4 for the mole fractions of main species (H_2, O_2, N_2 and OH). The calculated profiles agree quite well with the experimental data for both the flames. The numerical predictions were compared with the experimental measurements also along the radial direction. Because of lack of space, only comparisons at 3 mm and 10 mm for Flame F3 are reported in Fig. 5, but additional comparisons are reported in the Supplemental material (Figs. SM1 and SM2).

A fully 3D simulation of the F2 flame was performed and compared with the 2D axisymmetric simulation reported above. As expected, the two numerical simulations were found in perfect agreement each other, giving us an additional support about the reliability of the code.

3.2. CH_4/air coflow flames

The CH_4/air coflow flame experimentally and computationally studied by Bennett et al. [49] was numerically modeled for valida-
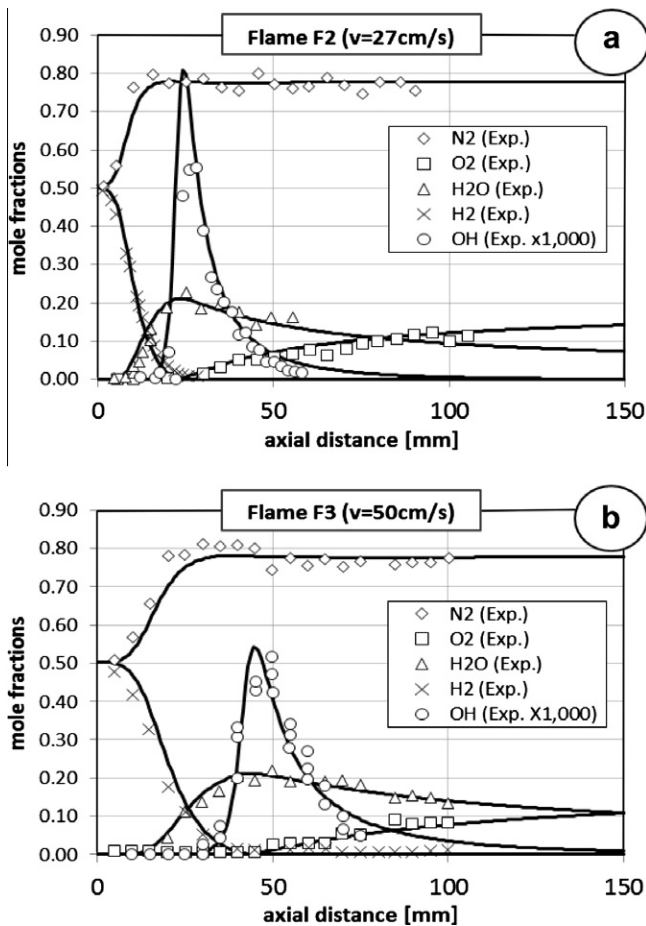
Fig. 4. H_2/N_2 coflow flames: comparison between experimental measurements [48] and numerical predictions in axial direction. (a) Flame F2; (b) Flame F3. Symbols are experimental data, lines are numerical predictions.

region immediately above the burner surface), using the POLIMI_HT1211 kinetic mechanism [43]. Further refinements of the grid did not result in any significant differences in the solution. Figure 6 reports the comparison between measurements and predictions along the centerline of the flame. The calculated height of the flame (defined as the axial location where the maximum of temperature occurs) is ~5.90 cm, in agreement with the experimental value of ~5.70 cm. In general, the calculated temperatures are lower than the corresponding experimental values by ~50–100 K, but this behavior is consistent with what was observed in [49] and in previous computational and experimental studies of a non-premixed methane/air flame [54]. The inflection points in the temperature profiles were attributed by Bennett et al. [49] to the deposition of soot particles on the thermocouple. Since in our kinetic models the formation of soot is not accounted for, the numerical profiles of Fig. 6 cannot reproduce this phenomenon. The overall agreement can be considered satisfactory. Main species (CH_4, O_2, H_2O and CO_2) are correctly predicted by the model, with the exception of H_2O, whose peak value is overestimated by ~10–15%. However, because of the difficulties in the calibration procedure (due to the low vapor pressure of H_2O at non-flame temperatures), the experimental measurements of H_2O reported in [49] were multiplied by a scale factor chosen such that the measured maximum concentration agreed with the maximum calculated value. Therefore, it seems more appropriate to compare the H_2O profiles only qualitatively. The profiles of C_2H_2 and OH are predicted very well by the numerical model and the peak values are correctly captured, both in terms of absolute values and positions. Mole fraction profiles of ketene (CH_2CO) and propene (C_3H_6) are in reasonable agreement with measurements, especially considering that the experimental data are accurate only within a factor of ~3.

3.3. C_2H_4/air coflow flames

The C_2H_4/air flame experimentally studied by McEnally and Pfefferle [50] was numerically modeled. The burner is the same adopted for the CH_4/air flame investigated by Bennett et al. [49] and described in the previous section. The inner jet (770 cm³/min) has a composition of 30% C_2H_4, 1% Ar and 69% N_2 (by volume). The coflow stream (44,000 cm³/min) is regular air. Both the streams are fed at ambient temperature and atmospheric pressure.

Also in this case, the numerical calculations were performed on a non-equispaced, structured mesh of 4800 cells, using the POLIMI_HT1211 kinetic mechanism [43]. Figure 7 reports the comparison between measurements and predictions along the centerline. Additional comparisons are provided as Supplemental material

tion purposes. The inner jet flows from a circular tube (i.d. 11.1 mm). The outer jet's inner diameter is 95.2 mm and the inner diameter of the cylindrical shield is 102 mm. The fuel (pure CH_4) is supplied through the inner jet at a flow rate of 330 cm³/min. The coflow stream (44,000 cm³/min) is regular air. Both the streams are fed at ambient temperature and atmospheric pressure.

The numerical calculations were performed on a non-equispaced, structured mesh of 4800 cells (with finest spacing in the
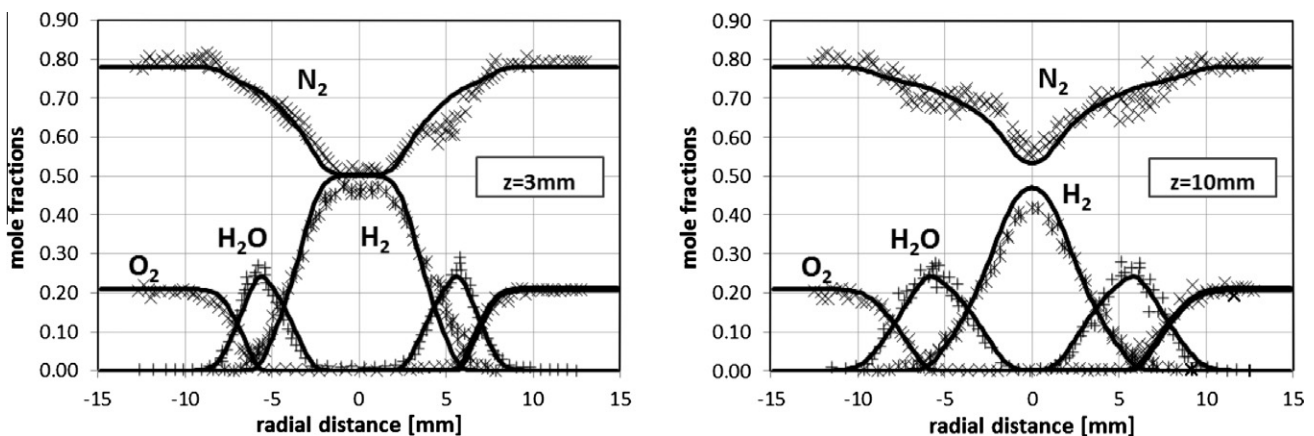

Fig. 5. H_2/N_2 coflow flames: comparison between experimental measurements [48] and numerical predictions in radial direction for F3 flame (50 cm/s) at z = 3 mm and z = 10 mm.
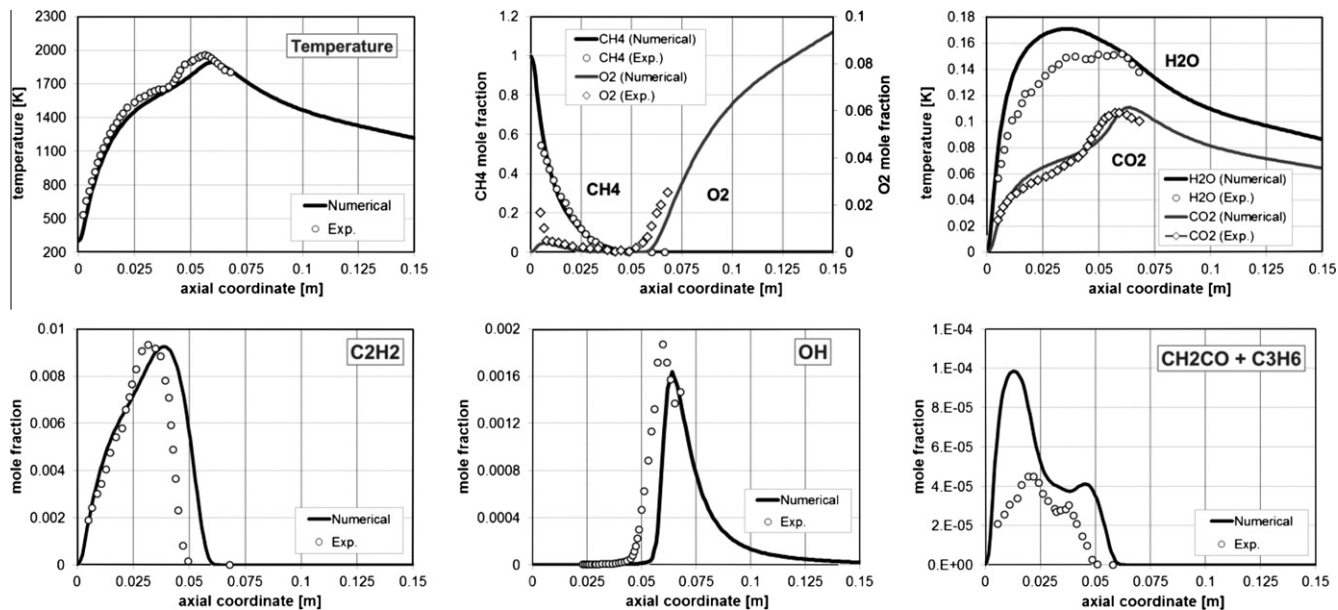
Fig. 6. CH_4/air coflow flame: comparison between experimental data [49] and numerical simulations along the centerline.

(Fig. SM3). The measured and calculated temperatures agree pretty well, with the exception of the region close to the central jet nozzle, where experimental values are ∼80–100 K higher. This can be attributed to the thermal boundary condition at the burner surface, where conduction and radiation caused a noticeable preheating of inlet streams. The maximum mole fraction of C_2H_2 is predicted quite well, but the peak is shifted towards a higher axial location. The experimental profiles of benzene (C_6H_6) and naphtalene (C_8H_{10}) are correctly captured by the numerical simulation. The simulation under-predicts the concentration of C_3H_4 isomers (allene and propyne) by a factor of ∼1.5, but an uncertainty factor of ∼3 in their measurements is acknowledged in [50]. A correct prediction of CH_2O is an important tool to measure the reliability of a numerical simulation, since it represents a key combustion intermediate. As reported in Fig. 7, the agreement is satisfactory,

although the CH_2O peak is over-estimated by a factor of ∼1.60 and appears more delayed with respect to the experimental data. The model predicts the concentrations of diacetylene (C_4H_2) and C_4H_6 (butadienes and butyne) quite well, together with the peak position, while the concentration of vinyl-acetylene (C_4H_4) is slightly under-predicted and its peak position shifted towards lower axial position.

3.4. Lifted methane/air diffusion flame

The computational framework was applied to a laminar diffusion flame, experimentally and numerically studied by Smooke et al. [52] and McEnally et al. [53]. The fuel mixture (65% CH_4, 35% N_2 by volume) is injected through a circular nozzle (i.d 4 mm), while coflow air enters through an annular region (i.d.
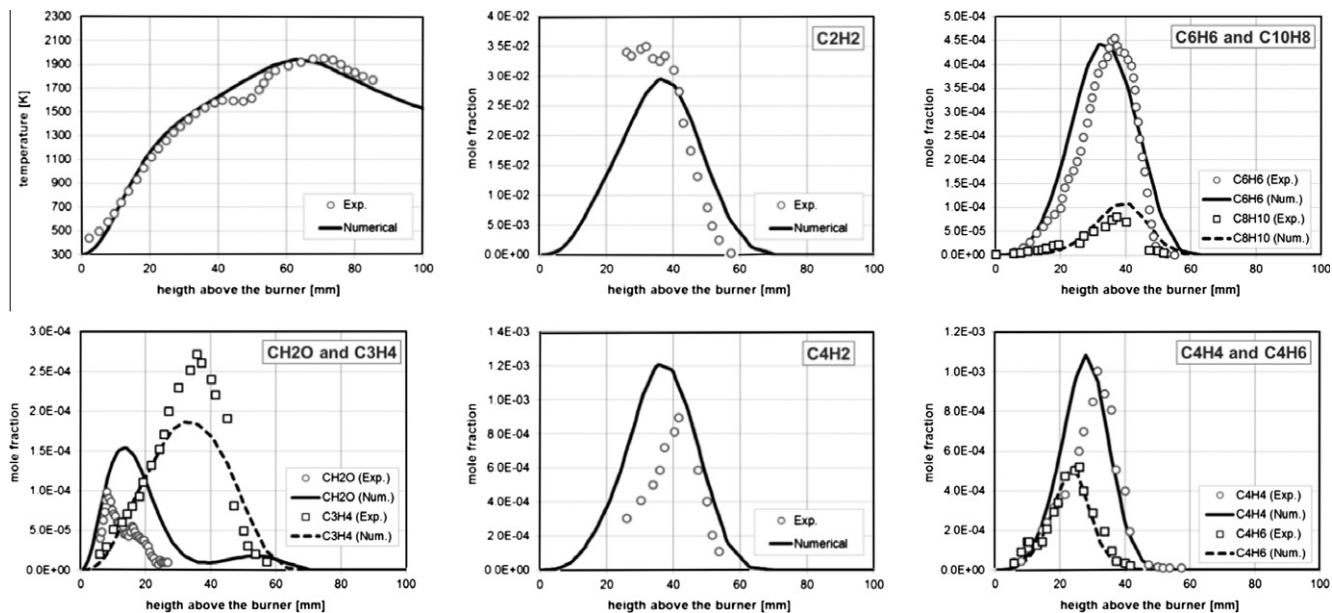

Fig. 7. C_2H_4/air coflow flame: comparison between experimental data [50] and numerical simulations along the centerline.

50 mm). Both the streams are at 298 K and atmospheric pressure. Experimental measurements of temperature, mole fractions of main (CH_4, O_2, CO, CO_2, H_2O, H_2) and minor species (C_2H_2, C_6H_6, CH_2CO) and NO are available.

The solution was calculated on a structured mesh with 6400 elements, plus two levels of local refinements on the region close to the fuel nozzle, for a total of ~12,000 cells. The calculations were performed using the `POLIMI_HT1211NOx` kinetic scheme [43]. The calculated map of temperature is reported in Fig. 8, together with the comparison with experimental data. The maximum temperatures are 1940 K, 1982 K and 2045 K for the computations, Rayleigh–Raman measurements and thermocouple measurements, respectively. As reported in [53], the thermocouple temperatures are substantially higher, especially in the core of the flame, as a consequence of heat conduction along the wire. The peak temperature does not occur at the center line, but in the "wings" at a radius of ~3.75 mm. Both from numerical and experimental data, it is evident that the flame is lifted from the burner surface. Experimental data show that the temperatures are close to room temperature from the burner surface to the height equal to ~6 mm, then they rise very rapidly to the maximum value. The calculated lift-off height is underestimated with respect to the measurements and it is only ~4 mm, but, from a structural point of view, the flame is correctly described and agrees satisfactorily with experimental maps. The flame heights, defined as the axial location where the maximum temperature occurs, are 34.5, 32.5 and 34 mm for the computations, Rayleigh–Raman and thermocouple measurements, respectively. In order to investigate the possible effect of the computational grid on the under-prediction of the lift-off height, calculations were repeated using finer meshes, with local, adaptive refinements (an example is reported in the Supplemental material

(Fig. SM4). However, even using very fine meshes (up to 30,000 cells), the predicted flame lift-off practically remained unchanged.

The 2D maps of mole fractions of major species are reported in Fig. 9, together with experimental data. The results show the expected behavior for a typical non-premixed flame, with CH_4 inside the flame front and O_2 outside it, and conversion first to CO and H_2 and then to CO_2 and H_2O. The model is able to capture the O_2 entrainment at the flame base, as clearly detected by the experimental measurements, both in terms of shape and magnitude. Similarly, experimental and numerical results show a slight outward-facing kink in the methane mole fraction at the lift-off height [53]. Comparison of CO and H_2 with experimental data is more difficult to judge, since the experimental CO and H_2 images contain more noise than the others. However, the magnitudes and the spatial distributions are correctly predicted by the numerical model.

Figure 10 reports the results for three species: acetylene (C_2H_2), benzene (C_6H_6), and ketene (CH_2CO). The agreement between the numerical results and the mass spectral measurements is not completely satisfactory, as observed for major species. In particular, the calculated maximum mole fractions along the axis are over-estimated: ~280 versus 63 ppm for benzene, ~8500 versus 4910 ppm for acetylene, and ~105 versus 74 ppm for ketene.

In Fig. 11 we report the calculated maps of mass fractions of NOx and HCN. Figure 12 show the comparison with experimental measurements of NO mole fraction profile along the centerline of the flame. NO increases along the axis and peaks at approximately ~35 mm, where the value of ~120 ppm is reached. The agreement with experimental data (peak of ~100 ppm at ~32 mm) is quite good, and the model is able to correctly capture the height above the burner (~10 mm) from which NO was experimentally detected. The NO reburning in the region between ~20 and ~30 mm appears over-estimated with respect to the experimental data. In order to understand if this strong reburning is a consequence of the kinetic scheme here adopted, the numerical simulations were repeated using the GRI30 kinetic mechanism [55]. The results (Fig. 12) are qualitatively quite similar: again, the peak is over-estimated and shifted at ~38 mm from the surface burner. Also for the GRI30, the presence of a reburning region (less pronounced) is evident while the peak of NO is larger. It is important to note that the reburning of NO occurs significantly through the reaction of NO with ketenyl radicals (HCCO) [56]. In the flame, these radicals are formed through the reaction of acetylene and O radicals. Therefore, it is likely that the observed overestimation of C_2H_2 and the influence of a larger amount of O radicals (associated to an overestimation of the entrainment of O_2 in this region of the flame) are responsible for the predicted important reduction of NO. In fact, the model predicts a large amount of ketene, which supports the hypothesis that also ketenyl radicals are overestimated.

4. Kinetic analysis of C_2H_4/CH_4 flames

In this section we numerically simulated the experiments performed by Roesler et al. [28] to investigate the effect of methane content on the formation of aromatic hydrocarbons in various fundamental configurations. In particular, after a short introduction about the motivations, in the first part the discussion is focused on the modeling of isothermal plug-flow reactors fed with mixtures of ethylene and methane in different amounts. Then, in the second part, the results of numerical modeling of a series of coflow diffusion flames fed with ethylene and methane diluted in nitrogen are presented and discussed from a kinetic point of view. To our knowledge, these are the first, systematic numerical simulations of such coflow flames with discussion of kinetic aspects.
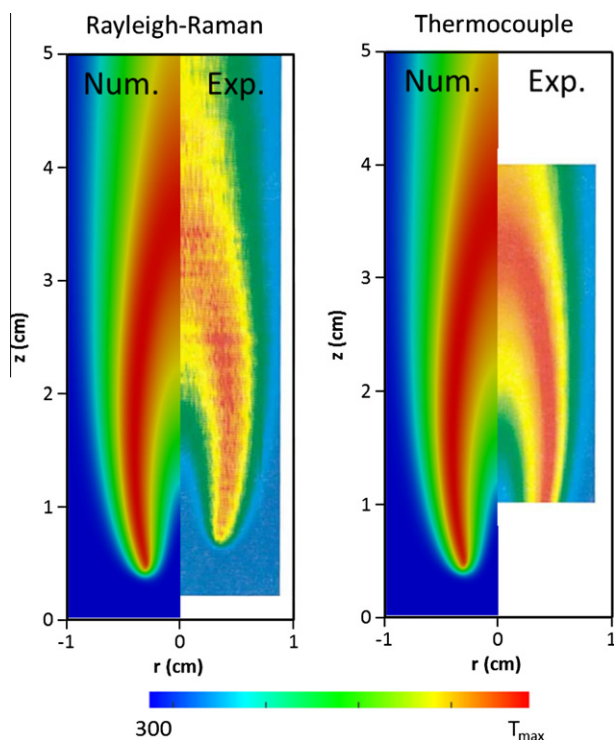

Fig. 8. CH_4/air lifted flame: 2D maps of temperature. The numerical results are compared with the experimental measurements of temperature obtained through the Rayleigh–Raman technique (left) or through a thermocouple (right). The maximum temperatures (T_{max}) are 1940 K, 1982 K and 2045 K for the computations, Rayleigh–Raman and thermocouple measurements, respectively. The experimental maps are adapted from the Fig. 1 reported in [53].
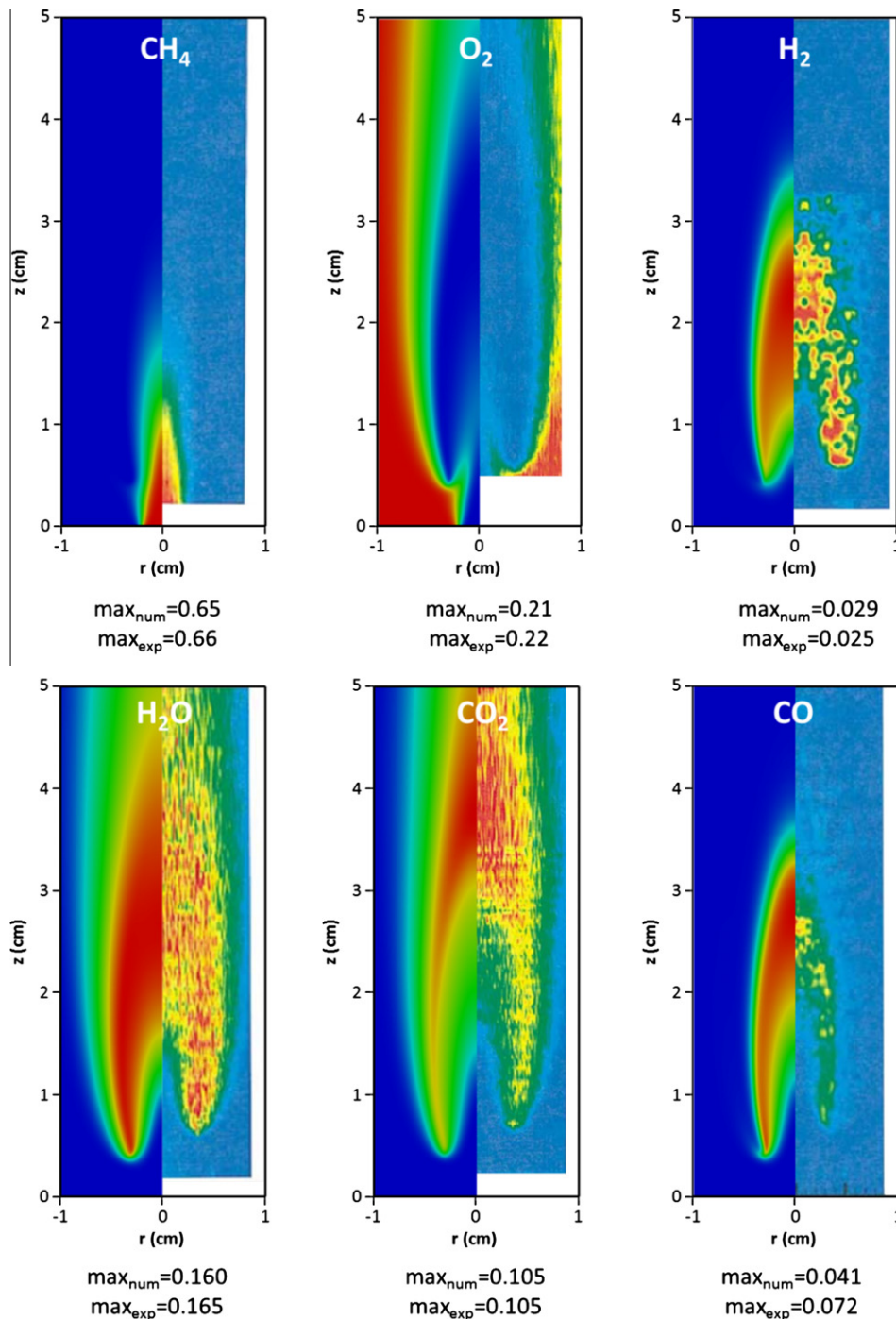
Fig. 9. CH_4/air lifted flame: 2D maps of mole fractions of major species. The numerical results (maps on the left) are compared with the experimental measurements (maps on the right).The experimental maps are adapted from the Figs. 2–7 reported in [53].

4.1. Motivation

The reduction of PAHs and soot formation in combustion processes requires the understanding of the chemical processes responsible for their formation and growth. There is a general agreement on the main features of the processes involved, as reviewed for instance by Ritcher and Howard [57] and others [58,59]: in fuel-rich and pyrolysis conditions, the formation of unsaturated light precursors (such as acetylene, propyne and allene) progressively brings to the formation of benzene and low-molecular weight PAHs through addition and cyclization reactions.

These species are the building blocks for the growth process which leads to the formation of soot [60]. Therefore, reactions involved in the formation of gaseous soot precursors, and in particular the formation of the first aromatic ring, have a key role in the chemical reaction pathways responsible for PAH growth and soot formation. Different mechanisms have been proposed in order to explain the formation of aromatic rings during fuel-rich combustion and they involve reactions between molecular precursors with even (C_2–C_4) and/or odd (C_1–C_3–C_5) number of carbon atoms. The relative importance and effectiveness of these different reaction paths depends on the combustion operative conditions and on the chemical
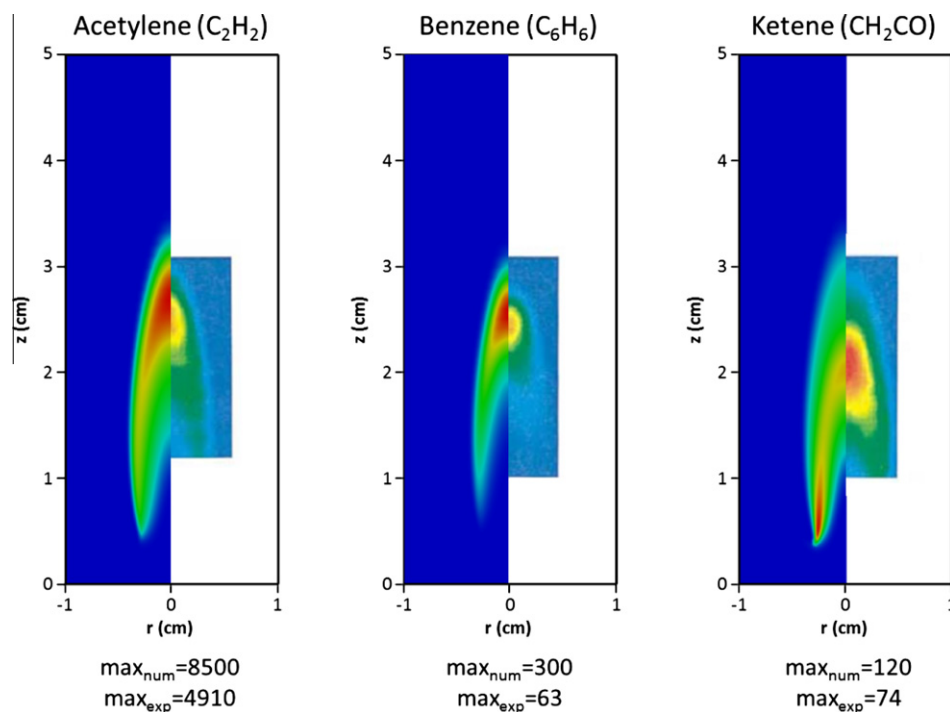
Fig. 10. CH_4/air lifted flame: 2D maps of mole fractions (in ppm) of non-fuel hydrocarbons. The numerical results (maps on the left) are compared with the experimental measurements (maps on the right).The experimental maps are adapted from the Figs. 8–10 reported in [53].
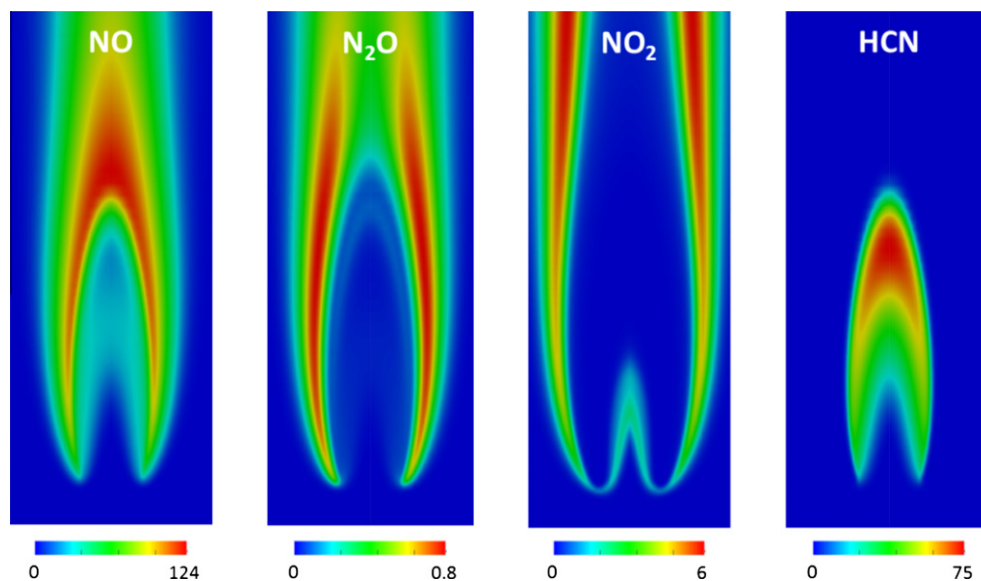

Fig. 11. CH_4/air lifted flame: 2D maps of calculated mass fractions (in ppm) of NOx and HCN.

composition of the fuel. A detailed kinetic analysis with the comparison between experimental and modeling results is essential to better understand at least the chemistry of PAH formation and this is the first step toward the development of new and cleaner hydrocarbon combustion processes.

4.2. Plug-flow reactors

Roesler et al. [28] studied the effect of methane addition on the formation of soot precursors in the rich oxidation of ethylene in a laminar flow reactor at 1430 K. The fuel was initially pure C_2H_4 and CH_4 was gradually added to the system maintaining the total car-

bon content (3% mole) and a C/O ratio equal 0.67. The relative concentrations of C_2H_4 and CH_4 are identified by the mixture parameter β (representing the fraction of fuel carbon injected as methane):

$$\beta = \frac{X_{CH_4}}{X_{CH_4} + 2X_{C_2H_4}} \qquad (14)$$

where X_i is the mole fraction of species i. In a previous paper, Roesler [61] already studied the rich combustion of pure methane ($\beta = 4.5$) in a laminar flow reactor and he theoretically verified that model predictions obtained using a one dimensional plug flow reactor are close to those of the corresponding 2D model accounting for
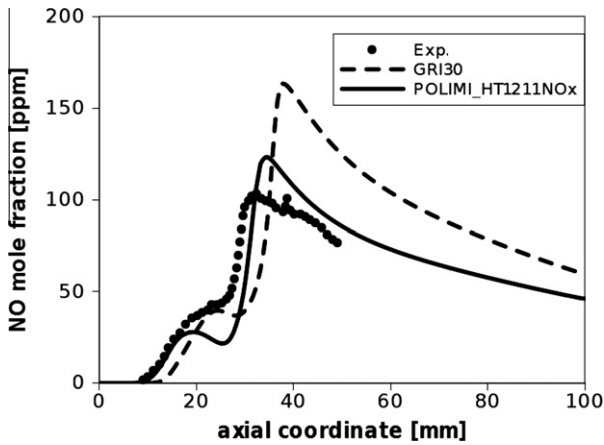
Fig. 12. CH_4/air lifted flame: NO mole fractions as a function of the distance along the centerline. The experimental measurements (points) [53] are compared with the numerical results obtained using the POLIMI_HT1211NOx (continuous line) [43] and the GRI3.0 kinetic schemes (dotted line) [55].

reactor [28]. The model properly captures the formation of major species, although H_2 is underestimated. This deviation can be attributed, at least partially, to the significant deposition of soot experimentally measured, which is not included in this modeling work. As expected, the addition of a more hydrogenated fuel has an enhancing effect on H_2 formation.

Figure 14 shows a reaction path analysis performed for a mixture with $\beta = 0.4$. It is possible to observe the important role of CH_3 radical which forms the ethyl radical and recombines to form ethane, followed by a significant formation of ethylene and acetylene. Moreover, the presence of CH_3 promotes the formation of a significant amount of C3 species through the reactions of CH_3 with vinyl radical and acetylene.

C_4H_4 is formed via $C_2H_3 + C_2H_2 = C_4H_4 + H$ and also $C_2H + C_2H_4 = C_4H_4 + H$ while diacetylene (C_4H_2) is mainly formed via H-abstraction reactions on C_4H_4 ($R + C_4H_4 = RH + C_4H_3$, $C_4H_3 = C_4H_2 + H$). For these reasons, it is evident that the addition of CH_4 reduces the amount of C2 species and therefore the tendency to form C4 species. Nevertheless, despite the decrease of C_2H_2 and C_4 species, CH_4 addition to the fuel mixture is responsible for the increase of PAH species.

The model in general correctly predicts the experimental trends, especially the significant increase of propyne and benzene when CH_4 is added to the system. Only phenylacetylene (not shown) and naphthalene formation are slightly overestimated by the model. The sensitivity analysis of Fig. 15 shows that, apart from
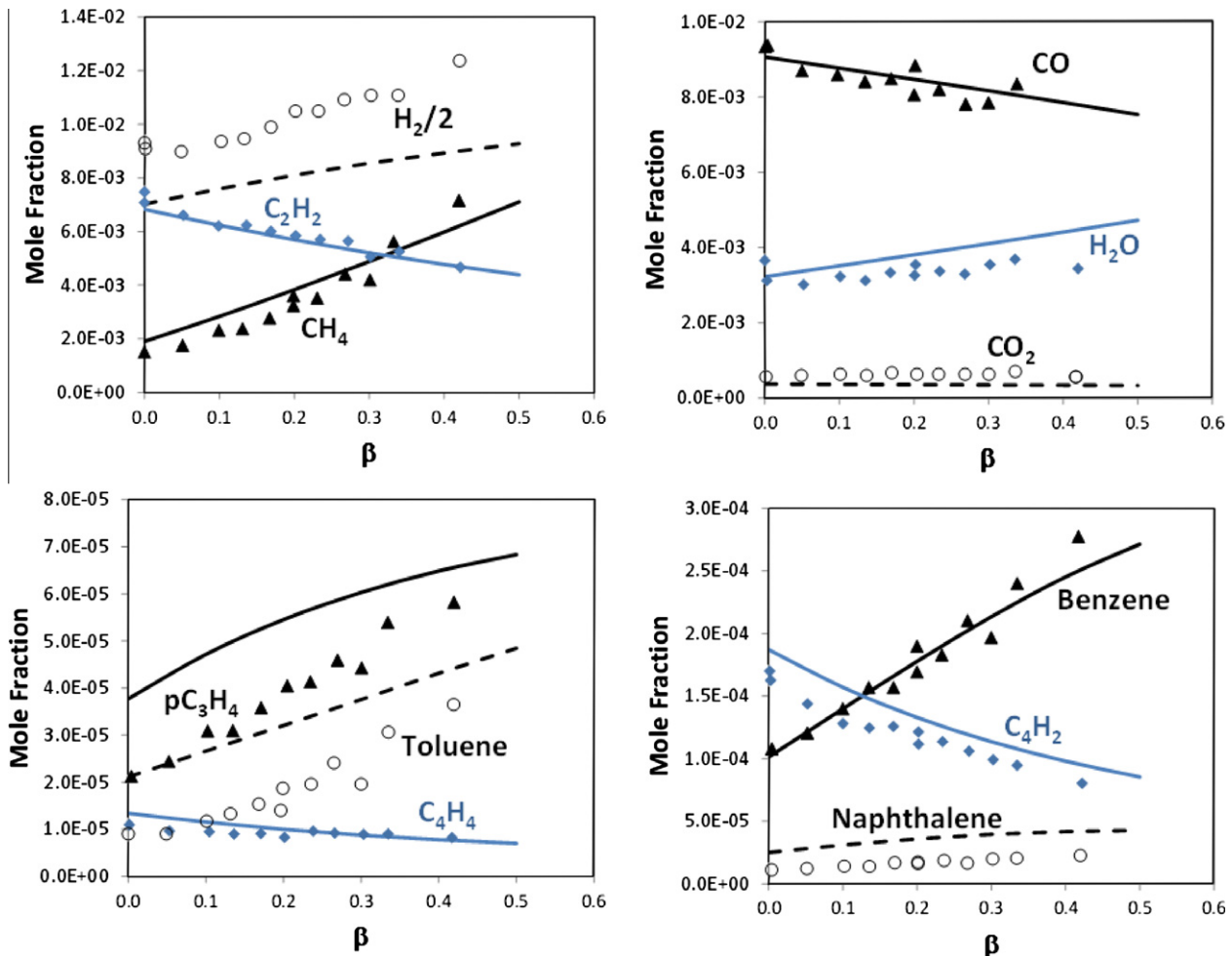
radial distributions. The pure methane case was already modeled and discussed by Granata et al. [62]. Therefore, we here focus on ethylene–methane mixtures.

Figure 13 shows the comparison between the predictions of the model and the experimental measurements in the laminar flow

Fig. 13. Laminar flow reactor: combustion of C_2H_4 and C_2H_4–CH_4 mixtures at $T = 1425$ K and C/O = 0.67. Outlet mole fractions versus the initial mixture parameter β. Comparison between model predictions (lines) and experimental measurements (points) [28].
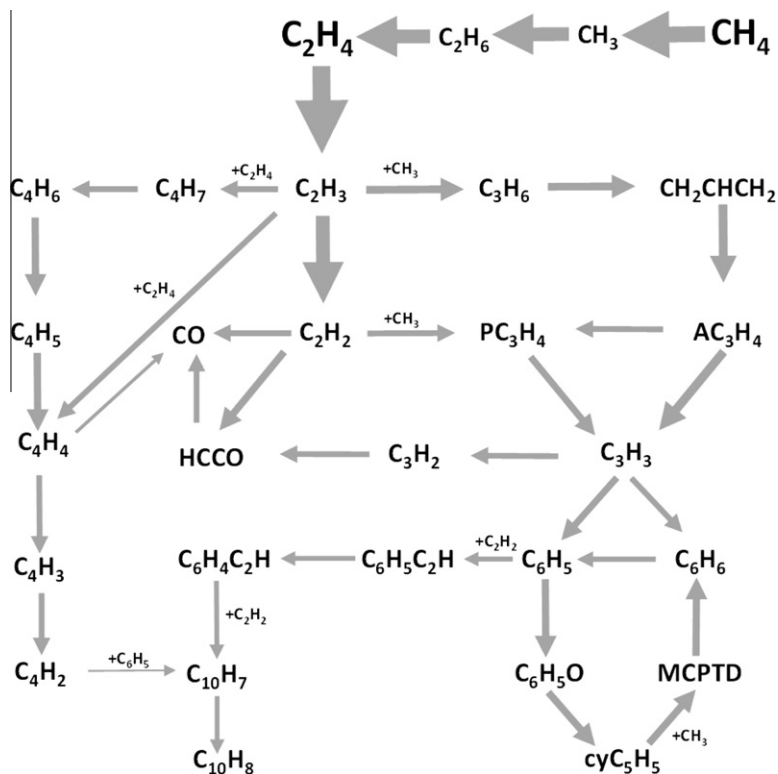
Fig. 14. Major reaction paths in the condition of Fig. 13 with $\beta = 0.4$. The thickness of the arrows is proportional to the rate of reaction.
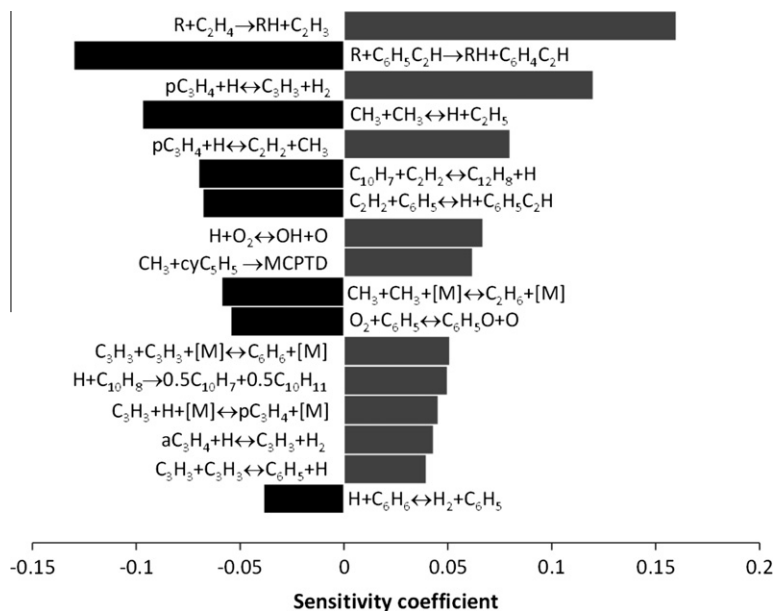

Fig. 15. Sensitivity coefficients benzene formation in the condition of Fig. 14 with $\beta = 0.4$.

the reactions controlling the reactivity of the system (H abstraction on ethylene and $H + O_2 = OH + O$), at $\beta = 0.4$ benzene formation has a positive sensitivity coefficient to the $C_3H_3 + C_3H_3$ reaction and to the decomposition reactions of allene and propyne to form C_3H_3. As already discussed by Cuoci et al. [63] and highlighted in Fig. 15, it is important to note that CH_3 radical and acetylene form a significant amount of propyne via the (reverse) reaction $pC_3H_4 + H = C_2H_2 + CH_3$. This reaction is a relevant source of propyne because of the high methyl radical concentration in the system.

Propyne subsequently forms propargyl radicals which then mainly forms benzene and phenyl radical. For this reason, reactions involving the consumption of methyl radical (recombination to form ethane and ethyl radicals) exhibit a negative sensitivity to benzene formation. The consumption of benzene via $H + C_6H_6 = C_6H_5 + H_2$ and the formation of phenoxy radicals ($O_2 + C_6H_5 = C_6H_5O + O$) also controls the amount of benzene in the system. In fact, phenoxy radicals subsequently forms cyclopentadienyl radical ($C_6H_5O \rightarrow cyC_5H_5 + CO$), which leads to cyclopentadiene

(cyC$_5$H$_5$ + H = cyC$_5$H$_6$) or methyl-cyclopentadiene (MCPTD) via the recombination with methyl radical. Since H-abstraction reactions on methyl-cyclopentadiene largely form benzene, the formation of MCPTD shows a large positive sensitivity coefficient. Finally, benzene formation shows a negative sensitivity to the reactions of phenyl radicals forming phenylacetylene and its consumption (C$_6$H$_5$ + C$_2$H$_2$ = C$_6$H$_5$C$_2$H and R + C$_6$H$_5$C$_2$H → RH + C$_6$H$_4$C$_2$H). Since this route is the major source of naphthalene, there is a competition between the amount of benzene and naphthalene in the system.

In these conditions, toluene is mainly formed via the recombination reaction CH$_3$ + C$_6$H$_5$. For this reason, the effect of CH$_4$ addition is quite evident.

Naphthalene formation largely occurs via H abstraction by naphthyl radicals, which are mainly formed through the reaction of phenyl (C$_6$H$_5$) and phenylacetylene radicals (C$_6$H$_4$C$_2$H) with C$_4$H$_2$ and C$_2$H$_2$, respectively. Therefore, naphthalene concentration is controlled by the competition between the HACA mechanism (C$_6$H$_5$ + C$_2$H$_2$ = C$_6$H$_5$C$_2$H and R + C$_6$H$_5$C$_2$H → RH + C$_6$H$_4$C$_2$H), the consumption of naphthalene (R + C$_{10}$H$_8$ → RH + C$_{10}$H$_7$, C$_{10}$H$_7$ + C$_2$H$_2$ = C$_{12}$H$_8$ + H) and the oxidation of C$_6$H$_5$.

Benzene formation predicted by the model agrees well with experimental measurements and indicates a synergistic effect of the addition of methane to ethylene. In order to better understand this effect, Fig. 16 shows the predicted profiles of different molecular and radical species along the flow reactor. Figure 16a shows that the maximum of acetylene moves from 0.007 to about 0.005 when methane is added to the mixture. As a consequence, the increase of benzene and PAHs cannot be attributed to the even mechanism, when methane is added to the mixture. The lower reactivity of the ethylene–methane mixtures is quite evident from the oxygen and CO profiles shown in Fig. 16c. The maximum of propargyl radical remains practically constant at about 15–20 ppm, as shown in Fig. 16b, but the different reactivity of the mixture has a significant effect also on the formation of minor species such as C$_3$H$_3$ and CH$_3$ radicals. It is relevant to observe that the addition of methane makes possible to significantly extend the lifetime of C$_3$H$_3$ in the reacting system (note the log scale in the panels of Fig. 16): the important role of propargyl radicals on the formation of the first aromatic ring and their enhanced lifetime explain the effect of CH$_4$ addition on benzene formation. The different reac-

tivity of the systems is also related to a larger initial peak of methyl radical observed in the case of pure ethylene oxidation (Fig. 16f), mainly due to the reaction O + C$_2$H$_4$ = CH$_3$ + HCO. When methane is added to the mixture, the benzene yield increases because the lower reactivity of the fuel mixture maintains a high concentration of propargyl radical for a longer time. This result clearly confirms that not only the concentration but also the lifetime of the radical are important factors [64].

4.3. C$_2$H$_4$/CH$_4$/N$_2$ coflow flames

The coflow flames experimentally studied by Roesler et al. [28] are fed with a mixture of C$_2$H$_4$, CH$_4$, Ar and N$_2$ in different amounts, using the same burner configuration adopted in [50]. The relative concentrations of C$_2$H$_4$ and CH$_4$ are identified by the mixture parameter β (see Eq. (14)). N$_2$ and Ar were added to maintain a constant, adiabatic temperature of 2230 K. The volumetric flow rates of C$_2$H$_4$, CH$_4$, Ar and N$_2$ are reported in [28].

The calculations were performed on a computational mesh with 4800 initial cells (locally refined up to ~9000 cells) using the POLIMI_HT1211 kinetic scheme [43].

Figure 17 shows the calculated maps of mole fractions of C$_2$H$_2$, C$_6$H$_6$, C$_{10}$H$_8$ and C$_{12}$H$_8$ for the flames at β = 0, 0.50 and 1.00. As better explained in the following, the peak concentrations of benzene and naphthalene show a non-monotonic behavior with the content of methane in the fuel mixture (in agreement with the experimental data), while the concentrations of C$_2$H$_2$ and C$_{12}$H$_8$ decreases monotonically with the β parameter. Additional maps and profiles of temperature and composition are provided in the Supplemental material (Figs. SM5 and SM6, respectively).

The maximum temperature and concentrations of species along the center-line were experimentally measured and reported as a function of β. A comparison with the numerical calculations is showed in Fig. 18. The measured temperatures have a minimum at $\beta \sim 0.60$, because of thermal radiation losses associated to the soot formation, which reaches a maximum at $\beta \sim 0.50$–0.60. The simulations do not consider soot formation and this can partially explain the flat predicted temperature profile. The maximum C$_2$H$_2$ concentration decreases as CH$_4$ is added, because C$_2$H$_4$ is replaced by a fuel that forms C$_2$H$_2$ less rapidly. The C$_3$H$_4$ (sum of a-C$_3$H$_4$ and p-C$_3$H$_4$) concentration increases,
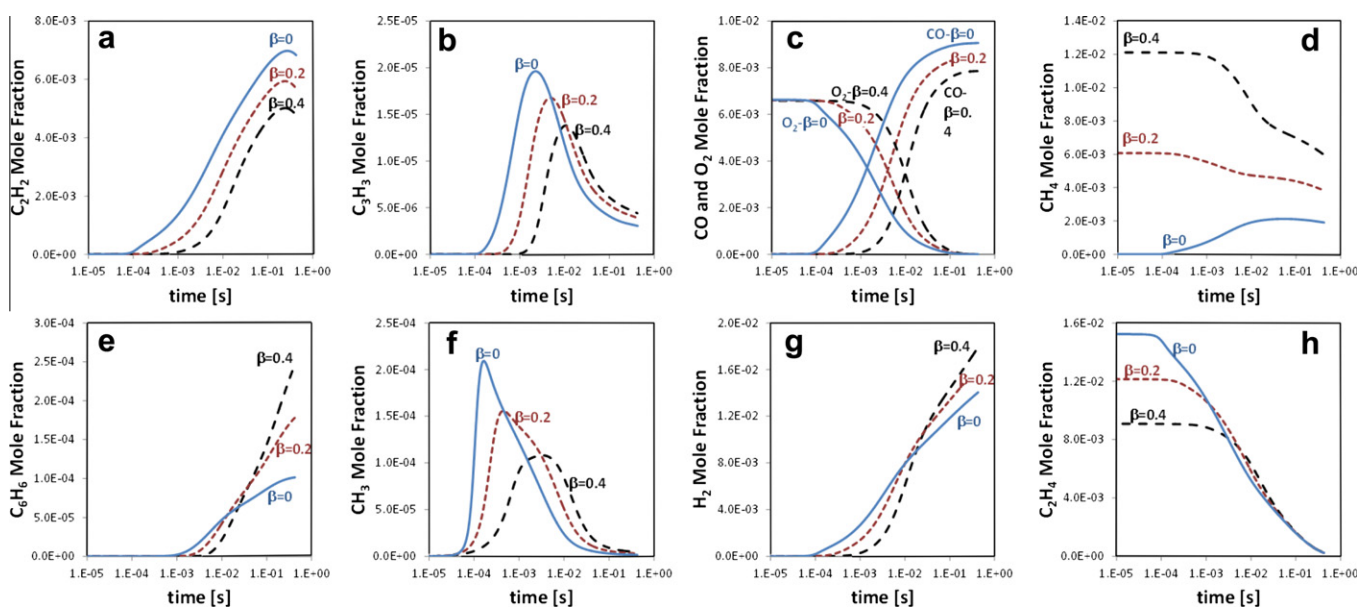

Fig. 16. Laminar flow reactor: combustion of ethylene and ethylene–methane mixtures. Mole fractions of relevant species versus residence time (log scale).
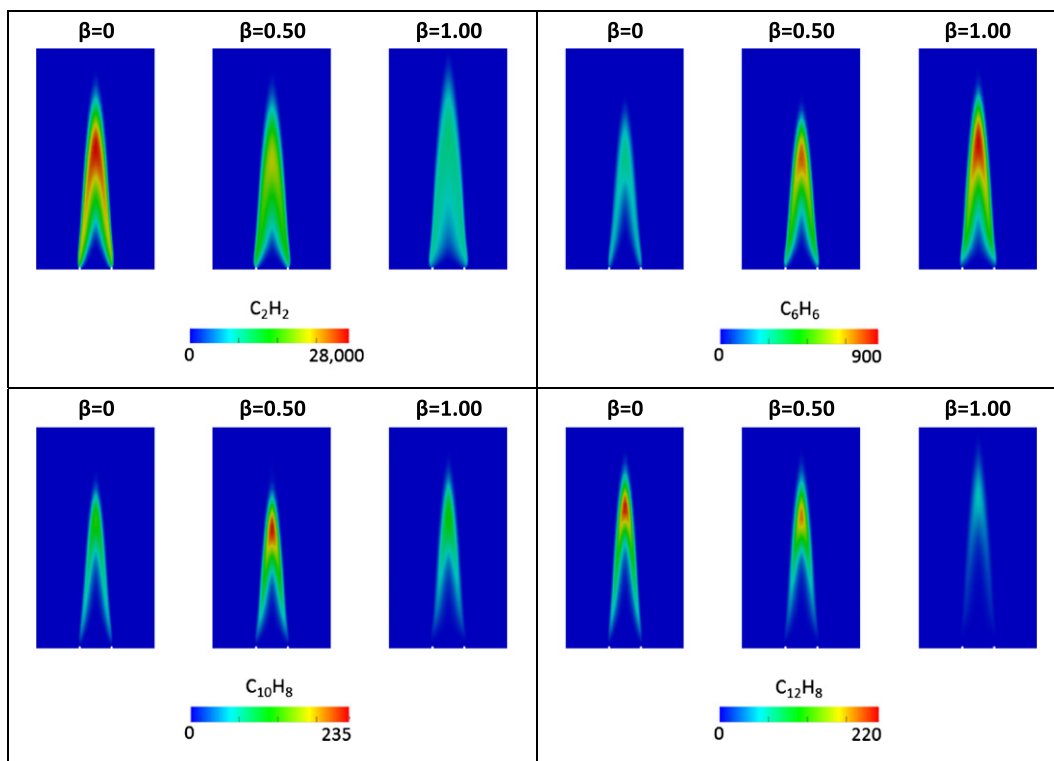
Fig. 17. $C_2H_4/CH_4/N_2$ coflow flames: calculated maps of mole fractions (in ppm) of selected species at different values of the mixture parameter β. The maps of species refer to a rectangular region of 42×80 mm.
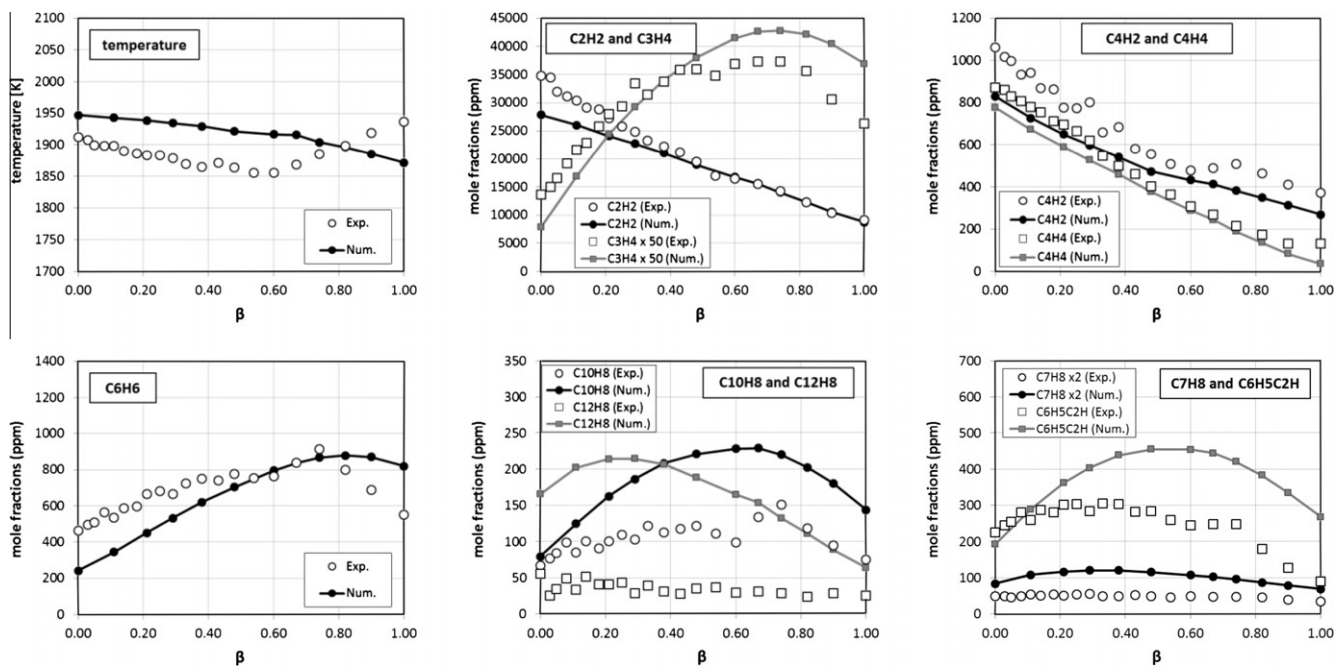

Fig. 18. $C_2H_4/CH_4/N_2$ coflow flames: comparison between experimental data [28] and numerical simulations. The maximum values along the center-line are reported as a function of the mixture parameter β.

since the increase in CH_4 is in proportion larger than the decrease in C_2H_2. The numerical predictions are able to capture these effects, even if the numerical maximum of C_3H_4 is less pronounced than the measurements and shifted towards larger values of β. The decrease of C_4H_2 and C_4H_4 with CH_4 addition is easily explained, since these species are mainly formed by the recombination of C_2-radicals and the reaction with C_2H_4. Benzene is correctly captured only for small values of mixture parameter

β, while for larger values there is an over-prediction by a factor of ~3. The measured flat profile of toluene (C_7H_8) was confirmed by the numerical simulations. The shapes of naphtalene ($C_{10}H_8$) and acenaphtalene ($C_{12}H_8$) profiles are satisfactorily predicted, even if the corresponding values are over-estimated. The overestimation of $C_{10}H_8$ and $C_{12}H_8$, also observed in the flow reactor cases, could be partially attributed to the limitations of the kinetic scheme, which is expected to underestimate the

consumption of such species, since it does not account for soot formation. An important role is played by the over-estimation of phenylacetylene ($C_6H_5C_2H$), which is a precursor of $C_{10}H_8$ and $C_{12}H_8$, as already discussed for the flow reactor case.

A more complete analysis on the observed deviations would require the coupling of a soot model, to evaluate the effect on the consumption of the soot precursors, related both to the chemical interactions (soot growth) and the effect of soot radiation on the flame temperature distribution. Nevertheless the predictions of the kinetic model agree reasonably with the experimental measurements, both in terms of absolute values and trends when the fuel mixture composition is changed. To our knowledge, this is the first, complete modeling of the experiments (flow reactor and laminar coflow flames) performed by Roesler et al. [28].

5. Conclusions

In this paper we presented `laminarSMOKE`, a new numerical framework for the modeling of laminar flames with detailed gas-phase chemistry. The framework is built on the top of the open-source `OpenFOAM`® code and therefore it is able to manage structured and unstructured meshes, with an arbitrary number of local refinements. In order to perform simulations with large and stiff kinetic schemes, the proposed solver is based on the operator-splitting approach.

The methodology was verified on premixed, flat flames, showing a satisfactory accuracy. The validation of the code was performed on several laminar, coflow flames. The agreement between experimental measurements and numerical results was satisfactory, demonstrating the feasibility and the accuracy of the operator-splitting approach (with detailed kinetics) for the modeling of laminar, reacting flows.

After its validation, the `laminarSMOKE` code was used to numerically simulate a set of coflow flames fed with mixtures of ethylene and methane in different amounts, in order to investigate the role of methane on the formation of aromatic hydrocarbons. In particular, the relative importance of even (C_2–C_4) and/or odd (C_1–C_3–C_5) reaction pathways leading to the formation of benzene and low molecular weight PAH was investigated using a detailed kinetic mechanism. The attention was preliminarily focused on the rich oxidation of ethylene and ethylene–methane mixtures in a isothermal flow reactor at high temperature. Model predictions were able to follow the synergistic effect of methane addition in ethylene combustion on the formation of benzene and consequently PAH and soot. The presence of methane in the combustion environment was found to be responsible for the increase of the propargyl radical lifetime, which is a key-factor for benzene formation via propargyl recombination.

In conclusion, the feasibility of the proposed `laminaSMOKE` solver was demonstrated through the numerical simulation of different coflow flames. The efforts were mainly focused on the creation of a numerical tool with the following features:

(1) Flexibility (structured and unstructured meshes, 2D and 3D domains, steady and unsteady problems).
(2) Easiness of use (pre and post-processing tools are provided by `OpenFOAM`®).
(3) Robustness (state of the art spatial discretization schemes provided by `OpenFOAM`®; modern ODE solvers for stiff problems).
(4) Ability to manage very large kinetic schemes (hundreds of species and thousands of reactions).

The numerical code is freely available on the web (http://www.opensmoke.polimi.it/) and open to external contribution from the combustion community.

Further developments will be focused on the reduction of the computational costs. Among several possibilities, the implementation of smart storage/retrieval methods [65] for a faster numerical integration of Eq. (12) seems a good solution to improve the performances of the code. A different solution is the adoption of the Directed Relation Graph (DRG) method for the automatic generation of skeletal, adapted mechanisms "on the fly". This method has been already applied by Tosatto et al. [66] on the simulation of axi-symmetric coflow flames for a variety of fuels and chemical mechanisms, showing excellent reduction of the computational costs. Additional work is required to implement more accurate radiative heat transfer models, in order to improve the predictive capabilities of the framework.

Appendix A. Verification procedure

A verification procedure was applied to the `laminarSMOKE`, in order to ensure that the equations are solved correctly and the numerical algorithms are implemented properly. However the numerical tests were not performed directly on laminar co-flow flames, but on a series of flat, laminar premixed flames, for the following two main reasons: (i) to save computational time (especially considering the large number of tests to be performed for a complete analysis); (ii) to compare the numerical solution with the solution obtained with `OpenSMOKE`®, a numerical code for the simulation of 1D flames, well verified and validated [26,43].

Several flames were used for the verification process, but only the results referring to a flame fed with a mixture of H_2 (39.7%), Ar (50%) and O_2 (10.3%) are here summarized. The reactants are fed at $T = 572$ K and $p = 0.0467$ atm at the velocity of 276 cm/s. The simulations were performed on a non-uniform 1D computational grid with 400 cells, using the `PolimiH2CO` kinetic scheme [44] and a centered, 2nd order discretization scheme. The numerical solution obtained with the `laminarSMOKE` code was compared with the solution from the `OpenSMOKE`® code, which solves the same equations using a fully-coupled method. Figure 19 reports
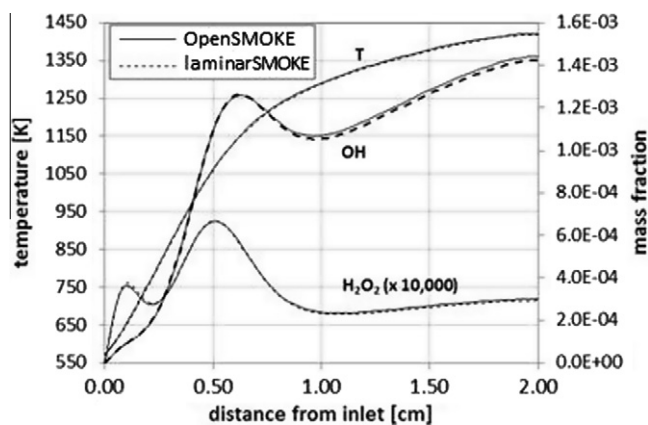

Fig. 19. Flat, laminar premixed flames fed with $H_2/Ar/O_2$ mixture: comparison between numerical solutions (continuous lines: `OpenSMOKE` code [43]; dotted lines: `laminarSMOKE` code).

Table 1
Verification of the numerical solutions: main flame features and post-processing results.

	Max values[a]				Mean values[b]		
	n = 1	n = 2	n = 3	∞	p	GCI (%)	Rn (%)
T (K)	1415.42	1417.4	1418.0	1418.29	1.71	0.023	75
H_2	0.01616	0.01615	0.01615	0.0161	1.72	0.0136	78
O_2	0.00037	0.00037	0.00037	0.00037	1.62	0.105	75
H_2O	0.14938	0.14944	0.14946	0.14946	1.64	0.0070	78
OH	0.00139	0.00140	0.00140	0.00140	1.58	0.137	69
H_2O_2	6.513E−08	6.624E−08	6.659E−08	6.675E−08	1.65	0.306	71
HO_2	1.246E−05	1.247E−05	1.247E−05	1.248E−05	1.68	0.0181	70
H	0.0036240	0.003627	0.003628	0.003629	1.55	0.0201	72
O	0.001651	0.001672	0.001679	0.001682	1.58	0.261	69

[a] For H_2 and O_2 the values at the outlet boundary are reported instead of maximum values.
[b] Global values of p and GCI are calculated by means of arithmetic and volumetric and averaging, respectively.

the calculated profiles of temperature and mass fractions of OH and H_2O_2. The maximum relative error between the two solutions is ∼0.22% for the temperature and ∼0.95% and ∼0.37% for OH and H_2O_2 mole fractions, respectively. The differences can be mainly attributed to the error introduced by the splitting procedure in the `laminarSMOKE` solver. An additional source of error could be attributed to the discretization procedure of the transport equations: the `OpenSMOKE`® code uses the finite-difference method, while the `laminarSMOKE` code is based on the finite-volume technique. Similar results can be observed also for all the species in the kinetic mechanism.

In order to better investigate the sensitivity of the simulation to the mesh spacing, additional tests were performed, based on the generalized Richardson extrapolation for h-refinement studies and on the Grid Convergence Index (GCI), as proposed by Roache [67]. Using this tools it is possible to estimate the order of accuracy (p) of the numerical solution and the error band where the grid independent solution is expected to be contained (uncertainty due to discretization GCI), therefore providing criteria on the reliability and credibility of these estimations. Additional details are reported in [67]. The h-refinement study was performed on 3 levels of refinement (n = 1, 2, 4), corresponding to 100, 200 and 400 grid cells. Local estimators of the GCI and p are calculated at the grid nodes (Richardson nodes) where monotone convergence is observed. The percentage of Richardson nodes (Rn) was found sufficiently large (higher than 69%). In Table 1, the main flame features, together with the GCI for temperature and mass fractions of species considered in the kinetic scheme are reported. The GCI was found to be sufficiently small to consider the error estimation reliable and the whole procedure correctly applied. As an example, the temperature has an average uncertainty of 0.0235% (which means ±0.33 K on the peak value). The global order of convergence accuracy (p) for each variable is in most cases larger than 1.55, which can be considered a satisfactory result, considering the stretch of the computational grid and the non-linear terms in the governing equations. Even if a lot of different discretization schemes are available in `OpenSMOKE`®, we did not perform a systematic and complete analysis about the discretization schemes. It is important to emphasize that, thanks to the numerical tools provided by `OpenSMOKE`®, the user has the possibility to choose the best discretization scheme for his purposes (i.e. the best compromise between accuracy and stability).

Appendix B. Supplementary material

Supplementary data associated with this article can be found, in the online version, at http://dx.doi.org/10.1016/j.combustflame.2013.01.011.

References

[1] R. Consul et al., Combust. Theor. Model. 7 (2003) 525–544.
[2] M.D. Smooke, R.E. Mitchell, D.E. Keyes, Combust. Sci. Technol. 67 (1989) 85–122.
[3] R.J. Kee, J.A. Miller, AIAA J. 16 (1978) 169–176.
[4] E.S. Oran, J.P. Boris, Numerical Simulation of Reactive Flows, Cambridge University Press, 2001.
[5] M.S. Day, J.B. Bell, Combust. Theor. Model. 4 (2000) 535–556.
[6] M. Duarte et al., SIAM J. Sci. Comput. 34 (1) (2012) 76–104.
[7] A. Nonaka, J.B. Bell, M.S. Day, C. Gilet, A.S. Almgren, M.L. Minion, Combust. Theor. Model. 16 (6) (2012) 1053–1088.
[8] A. Ern, C.C. Douglas, M.D. Smooke, Int. J. Supercomput. 9 (1995) 167–186.
[9] B.A.V. Bennett, M.D. Smooke, Combust. Theor. Model. 2 (3) (1998) 221–258.
[10] B.A.V. Bennett, M.D. Smooke, J. Comput. Phys. 151 (1999) 684–727.
[11] S.B. Dworkin, B.A.V. Bennett, M.D. Smooke, J. Comput. Phys. 215 (2006) 430–447.
[12] M.D. Smooke et al., Combust. Flame 143 (2005) 613–628.
[13] O.M. Knio, H.N. Najm, P.S. Wyckoff, J. Comput. Phys. 154 (1999) 428–467.
[14] M. Frenklach et al. <http://www.me.berkeley.edu/gri_mech/>.
[15] A. D'Anna, A. D'Alessio, J.H. Kent, Combust. Flame 125 (2001) 1196–1206.
[16] F. Liu et al., J. Quant. Spectrosc. Radiat. Transf. 73 (2002) 409–421.
[17] H. Guo et al., Combust. Theor. Model. 6 (2002) 173–187.
[18] S.V. Patankar, Numerical Heat Transfer and Fluid Flow, Taylor & Francis, London, 1980.
[19] M.R.J. Charest, C.P.T. Groth, O.L. Gulder, Combust. Theor. Model. 14 (6) (2010) 793–825.
[20] R.R. Dobbins, M.D. Smooke, Flow Turbul. Combust. 85 (2010) 763–799.
[21] R. Becker, M. Braack, R. Rannacher, Combust. Theor. Model. 3 (1999) 503–534.
[22] E. Burman, A. Ern, V. Giovangigli, Combust. Theor. Model. 8 (2004) 65–84.
[23] OpenFOAM, www.openfoam.org, 2011.
[24] G. Buzzi-Ferraris, D. Manca, Comput. Chem. Eng. 22 (11) (1998) 1595–1621.
[25] G. Buzzi-Ferraris, BzzMath 6.0 Numerical Libraries, 2010. <http://homes.chem.polimi.it/gbuzzi/index.htm>.
[26] A. Cuoci et al., Combust. Flame 156 (10) (2009) 2010–2022.
[27] A. Cuoci et al., OpenSMOKE: numerical modeling of reacting systems with detailed kinetic mechanisms, in: XXXIV Meeting of the Italian Section of the Combustion Institute, Rome, Italy, 2011.
[28] J.F. Roesler et al., Combust. Flame 134 (2003) 249–260.
[29] S. Chapman, T.G. Cowling, The Mathematical Theory of Non-Uniform Gases, Cambridge University Press, Cambridge, 1970.
[30] T.P. Coffee, J.M. Heimerl, Combust. Flame 43 (1981) 273–289.
[31] A. Ern, V. Giovangigli, Combust. Theor. Model. 2 (1998) 349–372.
[32] V. Giovangigli, Multicomponent Flow Modeling. MESST Series, Birkhauser Boston, 1999.
[33] G. Dixon-Lewis, Proc. Roy. Soc. 307 (1968) 111–135.
[34] R.J. Hall, J. Quant. Spectrosc. Radiat. Transf. 49 (1993) 517–523.
[35] Z. Ren, S.B. Pope, J. Comput. Phys. 227 (2008) 8165–8176.
[36] G. Strang, SIAM J. Num. Anal. 5 (1968) 506–517.
[37] D. Manca et al., Combust. Theor. Model. 5 (2001) 185–199.
[38] Y. Saad, Iterative Methods for Sparse Linear Systems, second ed., Society for Industrial and Applied Mathematics, Philadelphia, 2003.
[39] R.I. Issa, J. Comput. Phys. 62 (1986) 40–65.
[40] B. Sportisse, J. Comput. Phys. 161 (2000) 140–168.
[41] D.L. Ropp, J.N. Shadid, C.C. Ober, J. Comput. Phys. 194 (2004) 544–574.
[42] E. Ranzi et al., Ind. Eng. Chem. Res. 44 (14) (2005) 5170–5183.
[43] E. Ranzi et al., Prog. Energy Combust. Sci. 38 (4) (2012) 468–501.
[44] A. Frassoldati, T. Faravelli, E. Ranzi, The ignition, combustion and flame structure of carbon monoxide/hydrogen mixtures. Note 1: Detailed kinetic modeling of syngas combustion also in presence of nitrogen compounds, Int. J. Hydrogen Energy 32(15 SPEC. ISS.) (2007) 3471–3485.
[45] R.J. Kee, F. Rupley, J.A. Miller, Chemkin II: A Fortran Chemical Kinetics Package for the Analysis of Gas-phase Chemical Kinetics, Sandia Report SAND89-8009 – Sandia National Laboratories, 1989.

[46] H. Wang, M. Frenklach, Combust. Flame 96 (1994) 163–170.
[47] S.W. Benson, Thermochemical Kinetics, second ed., Wiley, New York, 1976.
[48] V.V. Toro et al., Proc. Combust. Inst. 30 (2005) 485–492.
[49] B.A.V. Bennett et al., Combust. Flame 123 (2000) 522–546.
[50] C.S. McEnally, L.D. Pfefferle, Combust. Flame 121 (2000) 575–592.
[51] B.A.V. Bennett et al., Combust. Flame 127 (2001) 2004–2022.
[52] M.D. Smooke et al., Proc. Combust. Inst. 26 (1996) 2161–2170.
[53] C.S. McEnally et al., Proc. Combust. Inst. 28 (2000) 2063–2070.
[54] M.D. Smooke et al., Combust. Flame 117 (1999) 117–139.
[55] G.P. Smith et al. <http://www.me.berkeley.edu/gri_mech/>.
[56] A. Frassoldati, T. Faravelli, E. Ranzi, Combust. Flame 135 (1–2) (2003) 97–112.
[57] H. Richter, J.B. Howard, Prog. Energy Combust. Sci. 26 (2000) 565–608.
[58] M. Frenklach, Phys. Chem. Chem. Phys. 4 (2002) 2028–2037.
[59] A. Frassoldati et al., Combust. Flame 158 (7) (2011) 1264–1276.
[60] A. D'Anna, Energy Fuels 22 (2008) 1610–1619.

[61] J.F. Roesler, Proc. Combust. Inst. 27 (1) (1998) 287–293.
[62] S. Granata et al., Formation of soot precursors in the rich combustion of hydrocarbon fuels, in: 10th International Congress on Combustion By-Products and their Health Effects, Ischia, Italy, June 17–20, 2007.
[63] Alberto Cuoci, Alessio Frassoldati, Tiziano Faravelli, Hanfeng Jin, Yizun Wang, Kuiwen Zhang, Peter. Glarborg, Fei Qib, Experimental and detailed kinetic modeling study of PAH formation in laminar co-flow methane diffusion flames, Proc. Combust. Inst. 34 (1) (2013) 1811–1818.
[64] E. Ranzi, Detailed kinetics of real fuel combustion: main paths to benzene and PAH formation, in: H. Bockhorn et al. (Eds.), Combustion Generated Fine Carbonaceous Particles, KIT Scientific Publishing, 2009.
[65] S.B. Pope, Combust. Theor. Model. 1 (1997) 41–63.
[66] L. Tosatto, B.A.V. Bennett, M.D. Smooke, Combust. Flame 158 (5) (2011) 820–835.
[67] P.J. Roache, J. Fluids Eng. 116 (1994) 404–413.